ACCSCIENCE PUBLISHING

International Journal of Bioprinting

RESEARCH ARTICLE

Construction of gelatin methacryloyl-based artificial skin substitutes with "small-micro" vascular networks via hybrid double-crosslinked coaxial and extrusion bioprinting

Yichen Luo[1,2], Dan Li[3], Cai Lin[4], Bin Zhang[1,2*], Hao Ding[5,6*] and Xue Zhou[1,2*]

[1]State Key Laboratory of Fluid Power and Mechatronic Systems, Zhejiang University, Hangzhou, Zhejiang 310058, China

[2]School of Mechanical Engineering, Zhejiang University, Hangzhou, Zhejiang 310058, China

[3]Department of Electro-Hydraulic Technology and Equipment Research Center, Binhai Industrial Technology Research Institute, Zhejiang University, Tianjin 300457, China

[4]Department of Burn, The First Affiliated Hospital of Wenzhou Medical University, Wenzhou, Zhejiang 325000, China

[5]Department of Cardiology, The Second Affiliated Hospital, School of Medicine, Zhejiang University, Hangzhou, Zhejiang 310009, China

[6]Cardiovascular Key Laboratory of Zhejiang Province, The Second Affiliated Hospital, School of Medicine, Zhejiang University, Hangzhou, Zhejiang 310009, China

(This article belongs to the *Special Issue*: *Biofabrication Breakthroughs: Innovation and Application in Bioprinting, Biomaterials, and Organoid*)

Abstract

The repair of deep skin defects involving subcutaneous tissue urgently requires vascularized skin substitutes that can provide immediate blood perfusion. However, existing engineering strategies struggle to construct multi-level vascular networks *in vitro*. This study aims to develop a multi-layered skin substitute with both biomimetic structure and physiological function, incorporating a perfusable "small-micro" hierarchical vascular system. We employed a composite coaxial–extrusion bioprinting strategy. First, a composite bioink consisting of 2% sodium alginate and 5% gelatin methacryloyl was formulated and evaluated for its printability and biocompatibility. Subsequently, using an ionic-photo dual-crosslinking coaxial printing technique, we fabricated subcutaneous small vessels with controllable dimensions and adequate mechanical properties. Finally, small vessels were integrated with an extrusion bioprinted dermal microvascular network and an epidermal layer to form a complete "small-micro" vascular pathway. This multi-layered construct was designed to mimic the stratified characteristics of natural skin. *In vitro* functional experiments confirmed that the epidermis possesses an excellent barrier function, and the subcutaneous small vessels demonstrated an effective capability for delivering drug molecules. The dual-crosslinking coaxial printing and composite manufacturing strategy proposed in this proof-of-concept study successfully constructed vascularized skin with a hierarchical tubular structure, offering a new solution with clinical translation potential for treating full-thickness skin defects.

***Corresponding authors:**
Xue Zhou
(zhouxue@zju.edu.cn)

Hao Ding
(11818166@zju.edu.cn)

Bin Zhang
(zbzju@zju.edu.cn)

Citation: Luo Y, Li D, Lin C, Zhang B, Ding H, Zhou X. Construction of gelatin methacryloyl-based artificial skin substitutes with "small-micro" vascular networks via hybrid double-crosslinked coaxial and extrusion bioprinting. *Int J Bioprint*. 2026;12(1):672-688. doi: 10.36922/IJB025490504

Received: December 2, 2025
Revised: January 5, 2026
Accepted: January 12, 2026
Published online: January 16, 2026

***Keywords*:** Artificial skin; Blood vessel; Coaxial printing; Gelatin methacryloyl; Three-dimensional bioprinting

1. Introduction

Deep tissue defects in the human body typically involve the loss of the epidermis and dermis, as well as damage to or absence of subcutaneous structures, including blood vessels, nerves, and the muscle layer.[1,2] The lack of functional vascular networks in traditional grafts leads to low graft survival rates, delayed healing, and impaired function in the damaged area.[3,4] Addressing these challenges requires the development of advanced skin substitutes featuring a multi-layered, vascularized structure that can restore the anatomical and physiological properties of the damaged tissue.

Recent advancements in bioprinting have offered promise for constructing complex tissues.[5] Various three-dimensional (3D) bioprinting modalities now enable the precise fabrication of biomimetic artificial skin structures. These techniques could effectively replicate the stratified epidermis–dermis architecture of native skin and integrate functional components such as vascular networks.[6–8] This diverse technological landscape has significantly expanded applications in wound healing and drug testing.[9,10] Among the materials used, gelatin methacryloyl (GelMA)[11] is widely employed as a core matrix material due to its excellent biocompatibility and tunable physical properties.[12,13] Sodium alginate (SA),[14] renowned for its rapid ionic crosslinking capability, effectively enhances the immediate shape fidelity and mechanical stability of printed structures.[15,16] Their excellent hydrophilicity and biocompatibility help regulate the local microenvironment, creating favorable conditions for cell growth and tissue regeneration.[17] Utilizing these materials, researchers have successfully created skin models mimicking the epidermis–dermis structure via techniques such as extrusion[13,18] and photopolymerization,[12,19] and have attempted to incorporate pre-vascularized components.[6,20,21]

Current mainstream strategies for introducing vascular structures into skin substitutes primarily fall into three categories. The pre-vascularization approach involves co-printing vascular endothelial cells with fibroblasts and other supporting cells within a blended bioink, relying on their self-assembly capability *in vivo* or *in vitro* to form microvascular networks.[22,23] For instance, Nuutila *et al.*[24] used a handheld bioprinter to deposit vascular endothelial growth factor (VEGF)-containing GelMA ink directly onto wounds, significantly promoting wound healing and neovascularization. A second approach leverages endothelial self-assembly by creating a permissive microenvironment within the printed dermal layer, enabling spontaneous lumen formation.[7,20] Choi *et al.*[12] used silk fibroin–gelatin ink for digital light processing printing to construct a pre-vascularized layer containing human umbilical vein endothelial cells (HUVECs) and human dermal fibroblasts, demonstrating cell proliferation within the ink. A third approach creates channels via sacrificial materials or coaxial printing. In sacrificial printing, a removable template (e.g., gelatin) is printed and later removed to form conduits that are endothelialized[8,25]; alternatively, coaxial printing can directly construct hollow tubular structures.[26] Thomas *et al.*[27] used projection stereolithography to simultaneously print a degradable sacrificial ink and hyaluronic acid methacrylate bioink, forming perfusable channels lined with HUVECs with a diameter of up to 360 μm. Ramasamy *et al.*[28] embedded a 3D-printed polycaprolactone mesh within acellular collagen and then sequentially printed bioinks containing human dermal fibroblasts and human adult keratinocytes to construct a full-thickness skin equivalent.

However, these strategies generally share two major limitations. Firstly, pre-vascularization often relies on the spontaneous tubulogenesis of endothelial cells within hydrogels, making it difficult to form structurally stable, dimensionally controllable subcutaneous small vessels *in vitro* that meet the requirements for surgical anastomosis with host vasculature. Secondly, they lack a hierarchical design mimicking the architecture of the native cutaneous vascular system, thereby struggling to achieve graded perfusion from small vessels to microvessels. This ultimately limits their efficacy in repairing deep defects.

To overcome these bottlenecks, this study proposes an innovative hybrid bioprinting strategy. Building upon our previously published multi-material extrusion printing technology,[29] we investigated and integrated coaxial printing methods to construct a multi-layered skin substitute featuring a "small-micro" hierarchical vascular network. Specifically, this study employs coaxial printing combined with an ionic-photo dual-crosslinking mechanism to precisely fabricate subcutaneous small vessels with excellent mechanical strength. A T-shaped microvascular network is designed within the dermal layer via extrusion printing, serving as a bridge connecting the small vessels to the superficial tissue. The ultimate goal is to integrate and validate the functional performance of a full-thickness skin model with multi-level vascular

networks. This strategy aims to develop and validate a hybrid bioprinting strategy for the integrated fabrication of a multi-layered skin substitute that incorporates a perfusable, hierarchical vascular network prototype, thereby restoring its crucial barrier and nutrient transport functions, providing the structural foundation for subsequent functional maturation.

2. Materials and methods

2.1. Preparation of vascular hydrogel inks and flowability measurement

Based on previous research findings,[30] 2% SA (Sigma-Aldrich, USA) and 5% GelMA (Sigma-Aldrich, USA) were identified as the optimal concentrations for formability and biocompatibility, respectively. Accordingly, five groups of hybrid hydrogels were prepared with the following compositions: 1% SA/5% GelMA, 2% SA/5% GelMA, 3% SA/5% GelMA, 2% SA/3% GelMA, and 2% SA/10% GelMA. The rheological properties of the hybrid hydrogel samples were measured using an MCR302 rotational rheometer (Anton Paar, Austria). The storage modulus (G′) and loss modulus (G″) were determined under conditions of a fixed frequency of 1 Hz and a temperature decreasing from 40°C to 4°C at a rate of 5°C/min. Additionally, the influence of temperature on viscosity was recorded as the temperature varied from 40°C to 4°C at a fixed shear rate of 50/s.

2.2. Cell culture

HUVECs (Cell Bank of the Chinese Academy of Sciences, China) and human foreskin fibroblasts (Fenghui Bio, China) were cultured in Dulbecco's Modified Eagle Medium/Nutrient Mixture F-12 (Gibco, USA) supplemented with 10% fetal bovine serum (Gibco, USA) and 1% penicillin/streptomycin. Human epidermal keratinocytes (KCs, Fenghui Bio, China) were cultured in defined keratinocyte serum-free medium (Gibco, USA) supplemented with epidermal growth factor (EGF) and bovine pituitary extract. All cells were maintained at 37°C under 5% carbon dioxide. HUVECs and HFF-1 were routinely passaged in tissue culture flasks and discarded after 8 and 12 passages, respectively. Primary KCs were used between passages 2 and 4 to ensure the retention of their proliferative and differentiation potential. The culture medium was changed every 2 days, and the cells were passaged when they reached 80%–90% confluence.

2.3. Biocompatibility of sodium alginate/gelatin methacryloyl composite hydrogels

The SA/GelMA bioinks (1%/5%, 2%/5%, 3%/5%, 2%/3%, 2%/10%) were prepared and uniformly coated into well plates. After complete crosslinking via immersion in calcium chloride solution and exposure to 405 nm light, endothelial cell suspensions of equal concentration and volume were added onto the material surfaces. Cell status on the material surface was observed after 7 days of incubation. SA/GelMA bioinks (1%/5%, 2%/5%, 3%/5%, 2%/3%, 2%/10%) loaded with green fluorescent protein-labeled HUVECs (1×10^6 cells/mL) were prepared. The bioinks were first ionically crosslinked by immersion in calcium chloride ($CaCl_2$; Sigma-Aldrich, USA), followed by complete photocuring under 405 nm light. Subsequently, the samples were immersed in a 20 mM ethylenediaminetetraacetic acid (EDTA; Gibco, USA) solution for 5 min to thoroughly degrade the SA component. After washing three times with complete culture medium to remove EDTA, the samples were incubated for 7 days, and cell spreading behavior was observed.

2.4. Simulation analysis of the flow field inside the coaxial printing nozzle

During the coaxial printing process, Fluent software (ANSYS 2022 R1, USA) was used to simulate the inner and outer flow channels separately to analyze fluid flow behavior. To simplify the simulation, the following assumptions were made regarding the fluid flow characteristics:

i The ink conforms to mass conservation, i.e., it is an incompressible fluid.

ii The fluid state is laminar, with a no-slip and no-penetration condition relative to the channel walls.

iii The inertial forces during flow are neglected.

A coaxial nozzle assembly consisting of an inner 22G needle (inner diameter 0.40 mm, outer diameter 0.45 mm) and an outer 17G needle (inner diameter 1.07 mm) was selected as the simulation object. The inner and outer flow channel models were constructed in SolidWorks 2021 (Dassault Systèmes, USA) and imported into Fluent for tetrahedral meshing. The ink was modeled as 2% SA, and the crosslinker as an aqueous $CaCl_2$ solution. The multiphase volume of fluid method was employed for solving the flow field.

2.5. Analysis and optimization of coaxial printing process parameters

A composite hydrogel consisting of 2% SA and 5% GelMA was prepared and printed using four nozzle combinations (G11–G15, G13–G18, G15–G20, and G17–G22; Shenzhen Deli Precision Technology Co., Ltd., China). A 0.5% $CaCl_2$ solution was used for ionic crosslinking, with the flow rates for both the inner and outer channels controlled at 2 mL/min. Apart from nozzle specifications, the influence of material flow rate can be divided into two aspects: the absolute flow rate values and their ratio. The G17–G22

nozzle combination, which met the diameter requirements for constructing small vessels, was selected for further printing tests. The flow rates for the inner and outer channels were sequentially decreased starting from 2 mL/min. Regarding the hydrogel-to-$CaCl_2$ flow rate ratio parameter, this factor alters the printed lumen structure by influencing the anti-collapse relationship between the two phases, with its effect being more pronounced at lower flow rates. Printing tests were conducted using the following hydrogel-to-$CaCl_2$ flow rate ratios: 0.5:1, 0.5:0.1, 0.5:0.3, 0.5:0.5, and 0.7:0.1 mL/min.

2.6. Construction of the small vessel intima

The subcutaneous small vessel consists of a bilayered structure comprising the vascular endothelium and the vascular wall, which cannot be achieved by coaxial printing alone. In this study, the lumen surface of the printed small vessel was first coated with Matrigel (Corning, USA). Subsequently, an endothelial cell suspension was injected into the lumen using a syringe. The vessel was positioned horizontally to allow the endothelial cells to settle and adhere to the inner wall of the vessel. The vessel was then rotated 90° every 5 min, repeating this process 5–10 times, before being transferred to a culture dish for incubation. Following this, the printed small vessel was embedded in 5% (w/v) GelMA containing HFF-1 cells to construct a tissue block containing the vascular structure. After 10 days of culture, the samples were embedded, sectioned, and characterized to assess the cross-sectional morphology of the printed small vessels.

2.7. Integrated construction of the multi-layered vascularized skin substitute

To achieve the integrated construction of the multi-layered vascularized skin, this study was based on the extrusion-based 3D bioprinting system (design principle shown in Figure S1) from previous research,[29] and integrated the coaxial printing nozzle into the printing system, as shown in Figure 1. The material supply for this nozzle is independently controlled by syringe pumps (Leadfluid, China) and shares the *XY*-axis system with conventional extrusion printheads, allowing for the one-step printing of multi-layered, vascularized skin substitutes. A 5% GelMA hydrogel containing HFF-1 (1×10^6 cells/mL) was printed as the subcutaneous layer. Small vessel structures containing HUVECs (1×10^6 cells/mL) were fabricated via coaxial printing. Subsequently, a 5% GelMA hydrogel containing HFF-1 cells was printed above this to construct the dermal

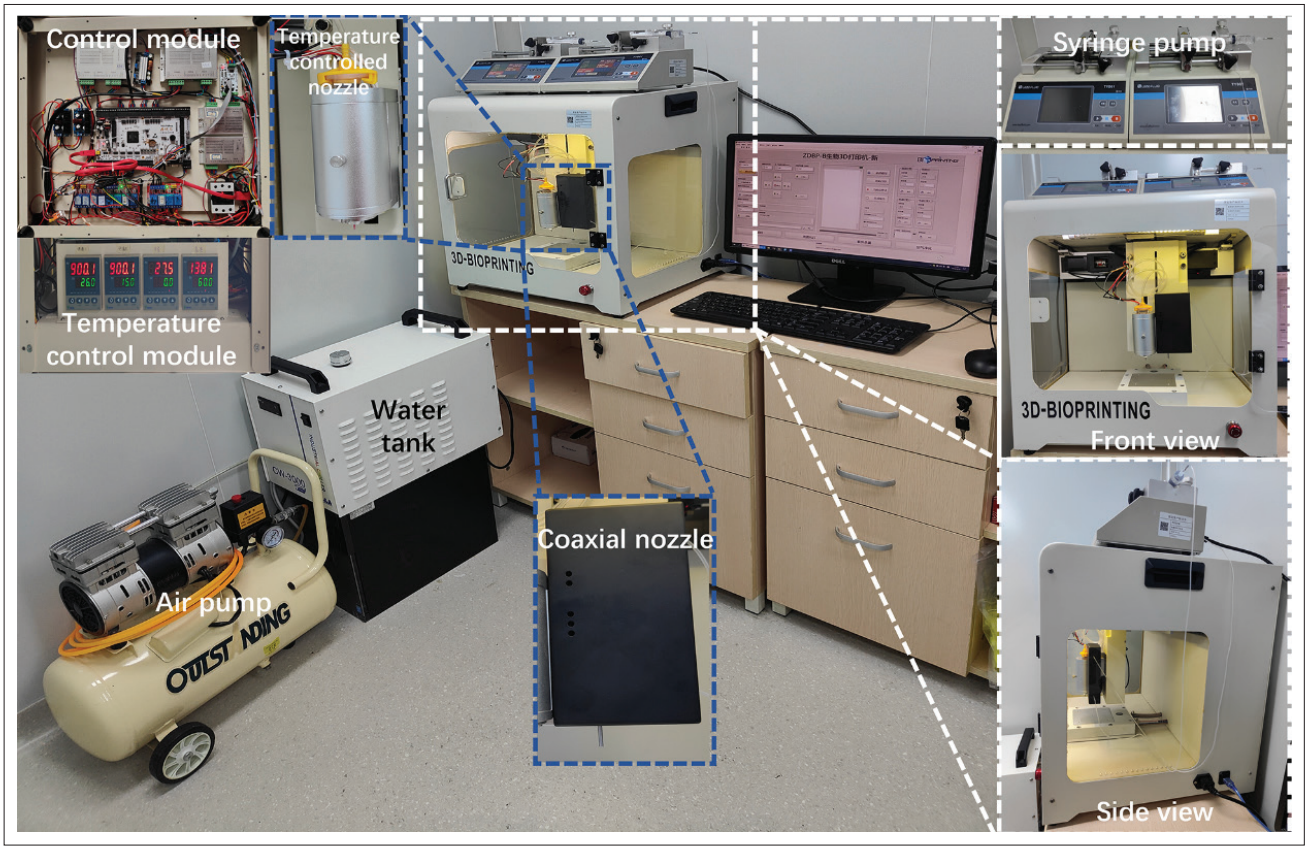

Figure 1. Composite construction system for the multi-layered vascularized skin substitute.

reticular layer. A 3% GelMA hydrogel containing HUVECs was extrusion-printed to form a microvascular network in the T-shaped papillary layer, serving as a bridge connecting the small vessels and the epidermis. Finally, a thin layer of 20% GelMA was printed as the epidermal base, onto which keratinocytes were seeded, while HUVECs were cultured within the vascular lumen.

2.8. Cell viability and morphology assessment

The HFF-1 cells (1.0×10^6 cells/mL) were added to 5%, 10%, 15%, and 20% concentrations of GelMA. Cell viability was assessed by measuring red or green fluorescent dye uptake using LIVE/DEAD® Viability/Cytotoxicity Kit (Abcam, UK). The samples were cultured in a humidified 5% carbon dioxide incubator at 37°C for 7 days. The fluorescence images of the cell-laden structures were collected using confocal laser scanning microscopy (ZEISS LSM780, Oberkochen, Germany). Cell proliferation was determined using Cell Counting Kit-8 assays (Medchemexpress, USA). The cells encapsulated in the GelMA were cultured in a humidified 5% carbon dioxide incubator at 37°C for 7 days. The samples were incubated at 37°C for 2 h, and cell viability was quantified by measuring absorbance at 450 nm using a microplate reader (RT-6100, Rayto, China).

2.9. F-actin fluorescent labeling

For the fluorescent staining of F-actin, the samples were washed twice in phosphate-buffered saline (PBS) and then fixed with 4% paraformaldehyde (Slarbio, China) for 10 min at room temperature. After a 3 × 10-min rinse with PBS, the samples were permeabilized with 5% Triton X-100 (Sigma-Aldrich, USA) for 3 min, washed thrice for 10 min in PBS, and stained with tetramethylrhodamine isothiocyanate phalloidin (Sigma-Aldrich, USA) for 30 min at 37°C in the dark. The samples were then washed three times for 5 min in PBS. The samples were then counterstained with 100 nM 4',6-diamidino-2-phenylindole (Solarbio, China) for 15 min at room temperature in the dark and then washed twice for 5 min in PBS. The images of the samples were observed using confocal stereo fluorescence microscope (M165FA, Leica, Germany) and analyzed using ImageJ version 1.54j (NIH, USA).

2.10. Barrier function assessment

2.10.1. Transepidermal water loss test

The vascularized skin was printed directly in Transwell inserts. After 14 days of culture, the inserts were removed. Surface culture medium was aspirated, and the inserts were inverted and placed into a sealed container. A predetermined amount of color-changing silica gel particles was placed at the bottom of the container, while deionized water was added to the porous membrane at the bottom of the inverted insert. The container was then sealed with sealing film. Silica gel particles were periodically removed to observe color changes and weighed.

2.10.2. Dextran–fluorescein isothiocyanate permeability assay

The vascularized skin was printed directly in Transwell inserts and cultured for 14 days. The original culture medium in the lower chamber was aspirated and replaced with PBS solution, ensuring the liquid level covered the skin's upper surface. A dextran–fluorescein isothiocyanate (Dextran-FITC; 40 kDa; Sigma-Aldrich, USA) solution prepared in PBS was added to the upper chamber. The fluorescent tracer permeated through the skin surface into the dermal layer and subsequently diffused into the lower chamber. The fluorescence intensity of the solution was measured at different time points under identical microscope parameters to analyze the barrier capacity of the skin samples.

2.10.3. Transepithelial electrical resistance measurement

Skin substitutes were printed directly in Transwell inserts and cultured for 14 days. Under sterile conditions, the old culture medium was aspirated from both the upper and lower chambers of the Transwell. Pre-warmed (37°C) fresh culture medium was added to both the upper and lower chambers, ensuring equal liquid levels. Transepithelial electrical resistance (TEER) measurements of the printed skin samples were performed using an EVOM voltohmmeter (Millicell ERS-2; Merck, USA).

2.11. Drug delivery function assessment

The vascularized skin was printed in Transwell inserts and cultured for 14 days. A 1 mg/mL solution of Dextran-FITC in PBS was prepared as a model drug molecule. Using a micro-syringe and flexible catheter, the Dextran-FITC solution was slowly injected into the inlet end of the constructed subcutaneous small vessel. Simultaneously with the initiation of perfusion, real-time time-lapse imaging of the vessel and the surrounding dermal matrix area was performed using stereo fluorescence microscope. Fluorescence images were captured at 0, 10, 20, and 30 min. ImageJ was used to measure the average fluorescence intensity within specific regions of interest outside the vessel in the captured image sequences and to quantify the diffusion rate of the fluorescent molecules.

2.12. Data processing methods

All data presented in this study were obtained from a minimum of three independent replicates. Experimental results are expressed as the arithmetic mean ± standard deviation of the mean (SEM). Outliers, defined as values

below Q1 − 1.5 × the interquartile range and above Q3 + 1.5 × the interquartile range, were excluded from the analysis. Statistical significance was analyzed using a one-way analysis of variance, with the Bonferroni method applied for multiple comparison corrections to adjust the *p*-values of individual tests. A *p*-value of ≤0.05 was considered statistically significant and marked with an asterisk (*). As the level of significance increased, the number of asterisks correspondingly increased.

3. Results and discussion

3.1. Rheological properties and biocompatibility of the composite hydrogel

The construction of stable and perfusable subcutaneous small vessels required a bioink that combines excellent printability/formability with good biocompatibility. To this end, we developed a composite hydrogel system comprising SA and GelMA and systematically evaluated its rheological properties and its ability to support HUVEC behavior. Rheological test results (Figure 2A) showed that all tested SA/GelMA composite hydrogel formulations exhibited typical thermosensitive behavior, with a defined gelation point (G' = G"). Figure 2B shows that the viscosity of all grouped inks decreased with increasing temperature, a property that can be utilized to control the extrusion behavior of the bioink by adjusting the temperature of the coaxial printhead. At the printing temperature, all formulated inks were in a flowing state with low viscosity, ensuring they could be smoothly extruded from the coaxial printhead and meeting the basic requirements for ink fluidity during the printing process.

Biocompatibility was another key criterion for ink screening. HUVEC adhesion experiments on the material surface are shown in Figure 2C. The results of Figure 2E indicate that when the SA proportion was too high (e.g., the 3% SA/5% GelMA and 2% SA/3% GelMA groups), cell adhesion rates were very low (all <0.6%), attributable to the inherent lack of cell adhesion sites in SA. In contrast, groups with higher GelMA content (1% SA/5% GelMA, 2% SA/5% GelMA, 2% SA/10% GelMA) exhibited relatively better cell adhesion, with the 2% SA/10% GelMA group showing the highest adhesion coverage (12.24 ± 1.41%), indicating that the RGD peptides in GelMA effectively promoted cell adhesion.

However, surface adhesion is only a two-dimensional characteristic; constructing 3D vascular structures requires investigation of cell spreading and tubulogenesis capability within the gel. We observed HUVEC tubulogenesis behavior after chelating and degrading the SA component with EDTA to expand the internal space of the gel. As shown in Figure 2D, after EDTA treatment, the 1% SA/5% GelMA, 2% SA/5% GelMA, and 2% SA/3% GelMA groups all supported significant HUVEC spreading and the formation of tubular structures. Notably, the 2% SA/3% GelMA group exhibited the best tubulogenesis capability, potentially due to its lower GelMA crosslinking density after pore expansion, which made it more conducive to cell extension and interaction (Figure 2F). In contrast, cells in the 2% SA/10% GelMA group mostly remained rounded, presumably because its crosslinked network was too dense; even after SA removal, the remaining cavity structure was insufficient to support cell spreading.

Integrating the above results, we balanced the ink's printability, cell adhesion, and 3D tubulogenesis capability. Although the 2% SA/3% GelMA group performed best in terms of intragel tubulogenesis, its low GelMA content might lead to insufficient mechanical strength of the final construct and poor surface cell adhesion. The 2% SA/10% GelMA group, while having good surface adhesion, had an internal structure unfavorable for 3D cellular functions. The 2% SA/5% GelMA formulation achieved the best balance among rheological properties, cell adhesion, and intragel tubulogenesis capability, and was therefore selected as the ideal bioink for subsequent coaxial printing.

3.2. Coaxial printing process optimization enables perfusable small vessels

We aimed to establish a stable and controllable coaxial printing process[31,32] to construct small vessels that met the dimensional requirements for subcutaneous vessels (lumen diameter 300–1000 μm) with structural integrity. After preliminary investigation of the ionic crosslinking process parameters between the SA/GelMA composite ink and the $CaCl_2$ solution, we found that an inappropriate flow rate ratio between the hydrogel and the $CaCl_2$ solution in the inner and outer channels prevented the stable formation of the tubular structure, potentially leading to clogging or fracture (Figure S2). Guided by simulations (Figure S3), we systematically investigated the effects of nozzle specifications, absolute flow rates, and the inner-to-outer flow rate ratio on the printed structure. The results indicated that the nozzle specification is the primary factor determining the vessel dimensions (Figure 3A). Using the G17–G22 nozzle combination at a flow rate of 2 mL/min, vessels with an outer diameter of 730.5 ± 14.9 μm and a wall thickness of 77.25 ± 5.26 μm could be stably fabricated, meeting the size and wall thickness requirements of small arteries. Maintaining the inner-to-outer flow rate ratio while decreasing the absolute flow rates effectively reduced the printed tube diameter (Figure 3B). This is attributed to fluid contraction being more susceptible to surface tension effects at lower flow rates, as Figure 3C intuitively illustrates. Furthermore, adjusting the flow rate ratio

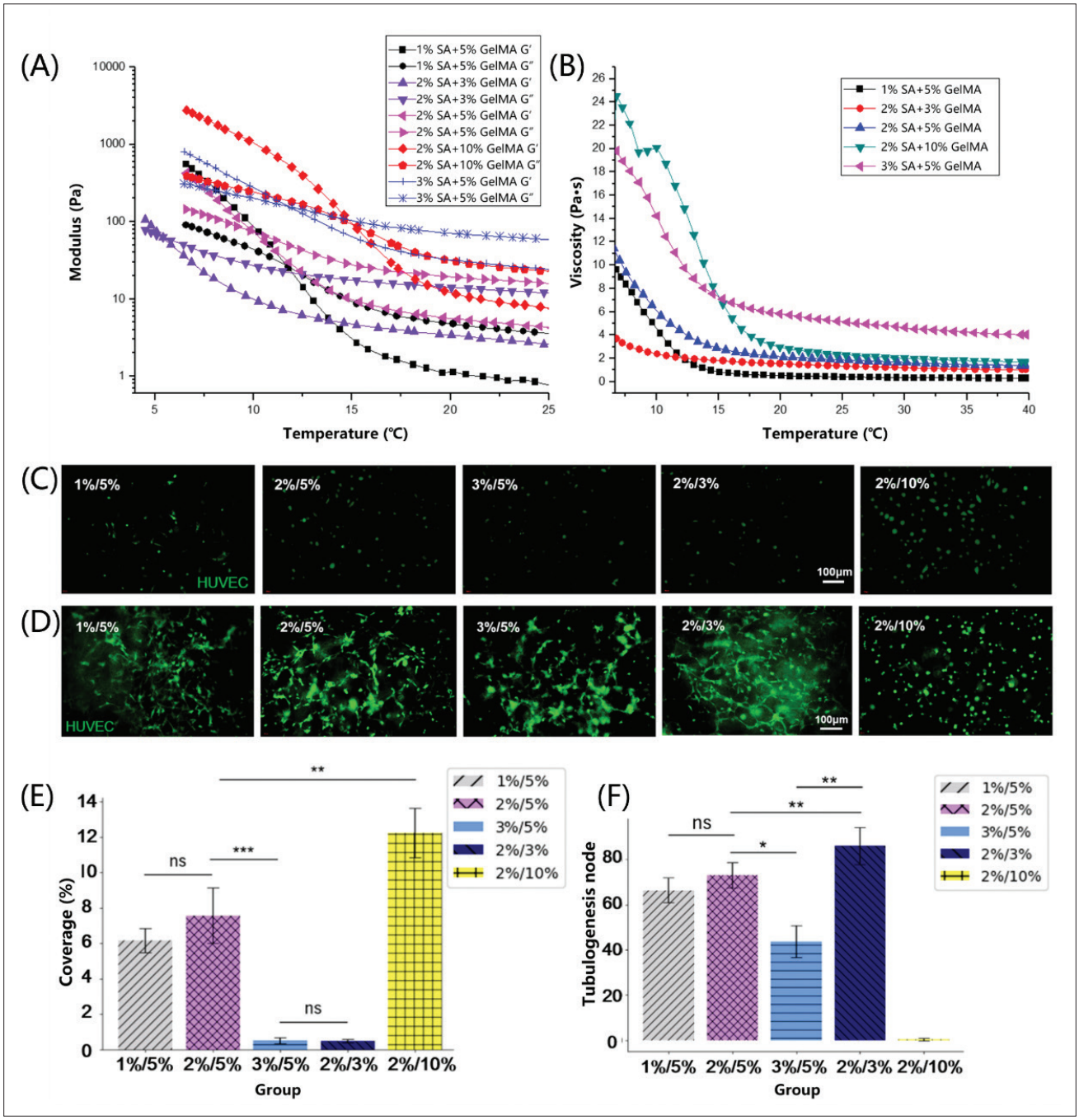

Figure 2. Biological characteristics of the composite hydrogels. (A) Modulus of different SA/GelMA hydrogels as a function of temperature. (B) Viscosity of different SA/GelMA hydrogels as a function of temperature. (C) HUVEC adhesion on the material surface. Scale bar: 100 μm; magnification: 100×. (D) HUVEC spreading within the hydrogels. (E) Coverage rate of HUVECs on the material surface. (F) The tubulogenesis node formed by HUVECs within the hydrogels. Data were analyzed using one-way analysis of variance and are presented as mean ± standard deviation (n = 3). Statistical significance determined at $^{*}p < 0.05$, $^{**}p < 0.01$, and $^{***}p < 0.001$, while ns indicates not significant. Abbreviations: GelMA, gelatin methacryloyl; HUVEC, human umbilical vein endothelial cell; SA, sodium alginate.

between the hydrogel and the crosslinker allowed precise modulation of the vessel wall thickness (Figure 3D). When the hydrogel flow rate was relatively high, the ability of the $CaCl_2$ stream to resist hydrogel retraction decreased, resulting in increased wall thickness; conversely, the wall thickness decreased as the flow rate decreased.

Formation relying solely on ionic crosslinking was still constrained by fluid surface tension at the nozzle, leading to lumen contraction and structural fluctuations.[33] To address this issue, we introduced an ionic-photo dual-crosslinking mechanism (Figure 3E). This strategy enabled the inner layer of the extruded hydrogel tube wall to undergo ionic crosslinking with $CaCl_2$, while the outer layer was simultaneously fixed by immediate photocuring, effectively counteracting the contraction effect (Figure 3F). Validation experiments showed that under the same printing parameters, the introduction of photocrosslinking increased the inner and outer diameters of the printed vessels by 18.5% and 18.8%, respectively, while the wall thickness remained unchanged (Figure 3G). Printing tests with varying flow rates yielded similar conclusions (Figure 3H). This characteristic can simulate the morphological differences between arteries and veins, offering the potential for constructing pathological models of arteriovenous malformations.

The dual-crosslinking strategy not only improved printing accuracy but also significantly enhanced the mechanical properties of the vessels. Tensile tests showed (Figure 4A) that the tensile modulus of the dual-crosslinked vessels reached 115.21 ± 6.34 kPa, representing a 119.49% increase compared to the 52.49 ± 4.79 kPa of the single-crosslinked vessels. Although this modulus is lower than that of human large arteries,[34] it meets the mechanical requirements for small animal vessels[35] and provides the necessary mechanical strength for subsequent surgery.[36] Meanwhile, we verified the patency and function of the printed vessels through dye perfusion experiments (Figure 4B). Red dye could completely perfuse an S-shaped lumen within 10 s without leakage, demonstrating its excellent liquid transport capability. In a small vessel grid scaffold constructed using this dual-crosslinking method, the dye also filled the entire network, indicating that this process maintains good lumen patency even when constructing complex, lengthy vascular structures (Figure 4C).

3.3. Construction and structural validation of the vascularized skin substitute

We further integrated coaxial printing with multi-material extrusion printing technology, aiming to achieve the integrated fabrication of a multi-layered skin substitute featuring a biomimetic "small-micro" vascular network (Figure 5A). The process involved printing a 5% GelMA hydrogel containing HFF-1 cells as the hypodermis/subcutaneous tissue layer. The small vessel structure containing HUVECs, obtained via coaxial printing, was embedded within this. Subsequently, a 5% GelMA hydrogel containing HFF-1 cells was printed above this to construct the dermal reticular layer. A 3% GelMA hydrogel containing HUVECs was then extrusion-printed to form a microvascular network in the papillary layer, specifically in a T-shaped zone, serving as the connection between the small vessels and the epidermis. Finally, a thin layer of 20% GelMA was printed as the epidermal base, onto which keratinocytes were seeded, while HUVECs were seeded on the surface of the vascular lumen, ultimately yielding the multi-layered, vascularized skin model (Figure 5B).

To evaluate the potential for endothelialization, we performed luminal seeding of HUVECs into the coaxially printed small vessels. The lumen surface was first coated with Matrigel to provide adhesion sites, followed by injection of a concentrated HUVEC suspension. Through a sequential rotation protocol, the cells were allowed to settle and adhere to the inner wall (Figure 6A(i)). After 5 days of culture, fluorescence staining revealed that HUVECs had adhered and spread across a substantial portion of the luminal surface, achieving a confluent cellular coverage (Figure 6A(ii, iii)). Quantitative analysis of the cell attachment area revealed that the attached area reached its peak after 5 days of culture, approximately four times the initial value, indicating that the intima had essentially formed (Figure 6A(iv)). This demonstrates the feasibility of our printed tubular structures as scaffolds for endothelial lining, highlighting their potential for subsequent vascular maturation. Embedding the printed small vessels within a fibroblast–GelMA matrix for sectioning and observation, 4',6-diamidino-2-phenylindol staining confirmed the presence of the hollow lumen structure (Figure 6B), although mechanical compression during sectioning caused slight distortion of its circularity.

Cross-sectional fluorescence analysis of the integrally printed construct confirmed the spatial organization achieved by our hybrid printing strategy (Figure 6C). The architecture displayed a multi-layered cellular distribution, suggesting it may correspond to the anatomical layers of skin: hypodermis, the cell-dense dermal layers, and the superficial epidermal layer. More importantly, the staining results clearly showed that the coaxially printed small vessels in the hypodermis were structurally connected to the T-shaped microvascular network formed by HUVECs via intervening cell clusters. This observation confirmed that our printing strategy successfully constructed a multi-level network ranging from the subcutaneous small

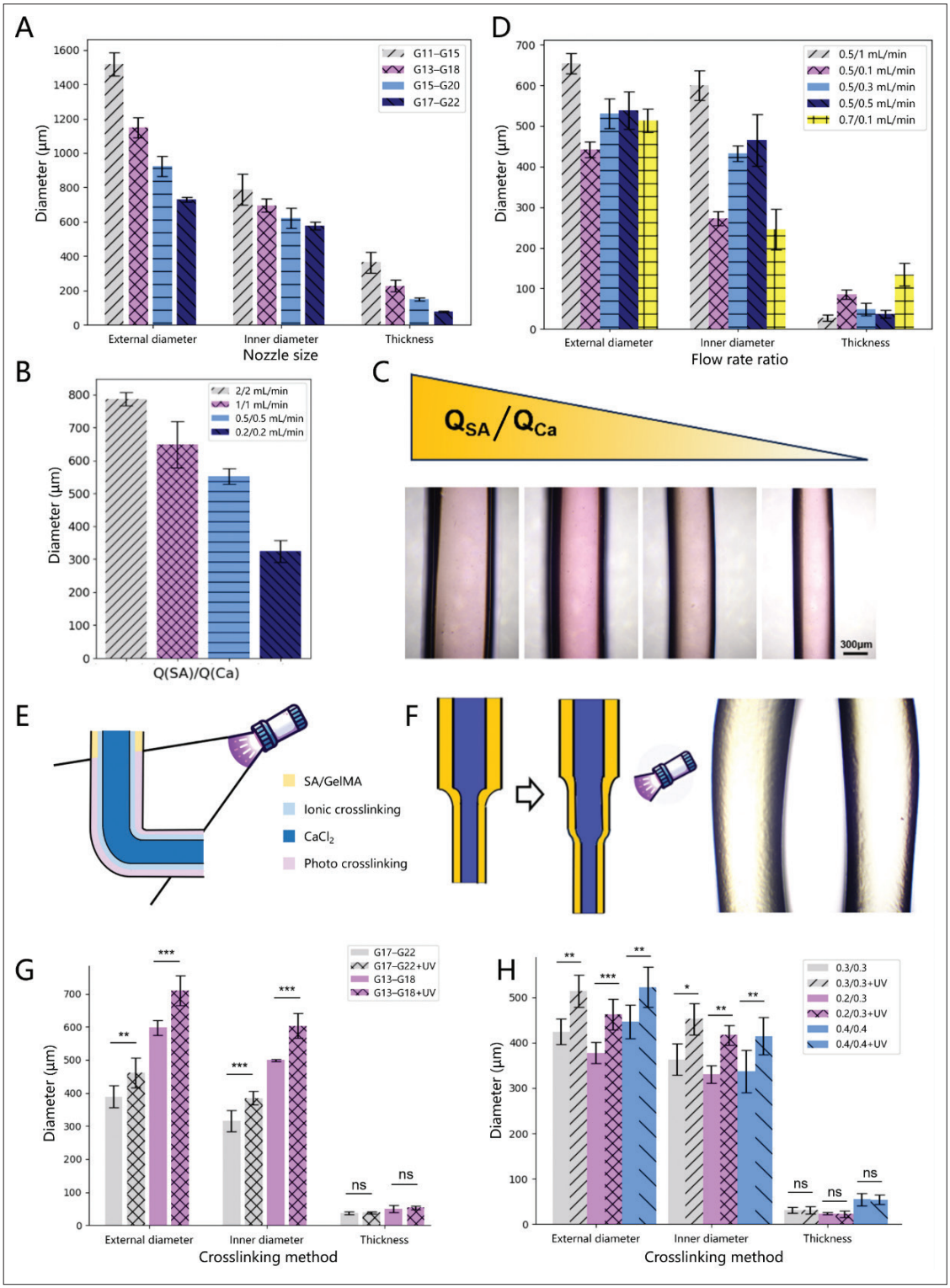

Figure 3. Optimization of coaxial printing nozzle parameters. (A) Vessel dimensions under different nozzle specifications and (B) different hydrogel flow rates. (C) Representative images of vessels printed at different hydrogel flow rates. Scale bar: 300 μm. (D) Vessel dimensions under different inner-to-outer flow rate ratios. (E) Ionic-photo dual-crosslinking schematic. (F) Comparison showing the enlarged lumen resulting from the dual-crosslinking strategy. (G) Vessel dimensions after introducing dual-crosslinking under different nozzle specifications and (H) different hydrogel flow rates. Data were analyzed using one-way analysis of variance and are presented as mean ± standard deviation ($n = 3$). Statistical significance determined at $^{*}p < 0.05$, $^{**}p < 0.01$, and $^{***}p < 0.001$, while ns indicates not significant. Abbreviations: $CaCl_2$, calcium chloride; GelMA, gelatin methacryloyl; SA, sodium alginate; UV, ultraviolet.

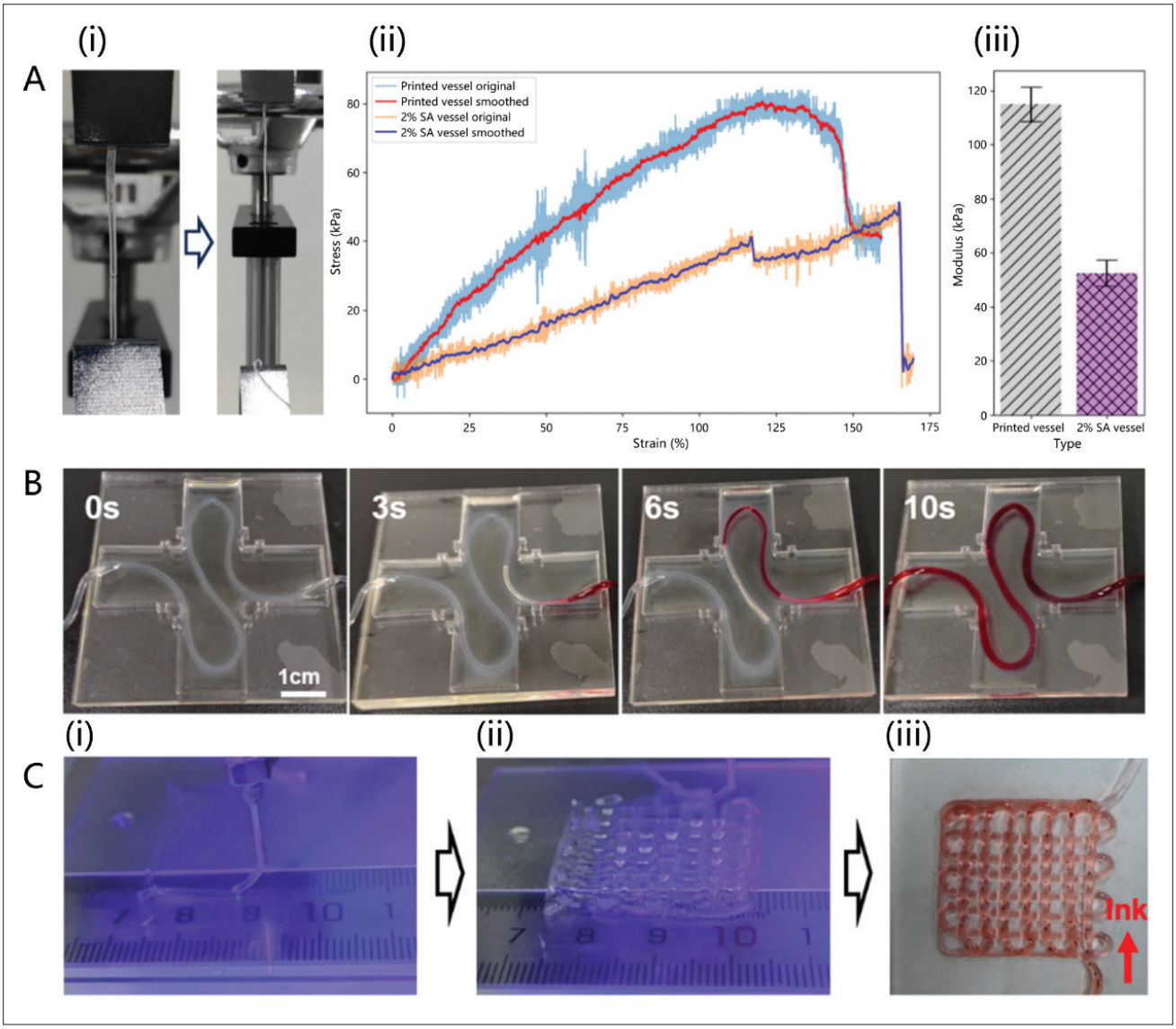

Figure 4. Characterization of coaxial-printed small vessel performance. (A) Mechanical properties of small vessels: (i) tensile testing, (ii) stress–strain curves, (iii) elastic modulus of the vessels. (B) Perfusion of vessels with red dye. Scale bar: 1 cm. (C) Small vessel grid scaffold: (i) printing initiation, (ii) upon printing completion, (iii) perfusion with red dye. Data were analyzed using one-way analysis of variance and are presented as mean ± standard deviation ($n = 3$). Statistical significance determined at $^{*}p < 0.05$, $^{**}p < 0.01$, and $^{***}p < 0.001$, while ns indicates not significant. Abbreviation: SA, sodium alginate.

vessels to the dermal microvessels, closely mimicking the hierarchical distribution of the vascular system in native skin. The current model provides the spatial organization of different cell types. However, achieving precise histological stratification and mature epidermal differentiation will be a key objective for the next stage of model refinement.

3.4. *In vitro* validation of the skin substitute

The structural biomimicry of the construct serves as the foundation for achieving its intended functions. To verify whether this multi-layered vascularized skin substitute possesses the key physiological functions of native skin, we conducted a series of *in vitro* experiments, focusing on evaluating its physical barrier function and the substance transport potential of the subcutaneous vascular network. The coaxial printing process developed in this work, combined with the previously reported layer-by-layer printing method,[29] forms a composite strategy for fabricating a multi-layered vascularized skin substitute, which was ultimately constructed and functionally validated. We established four experimental groups: the no epidermis group contained only the dermal layer, lacking

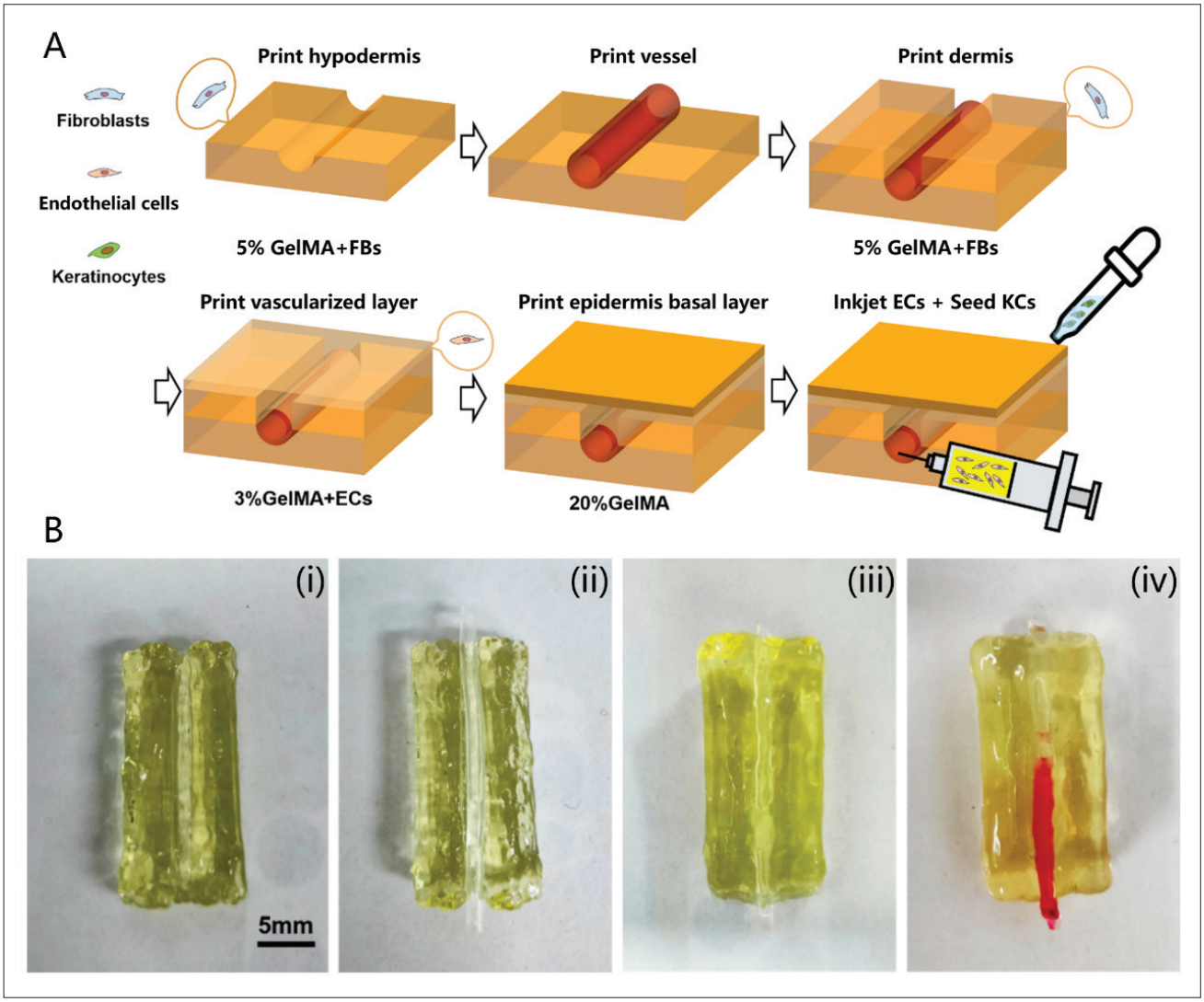

Figure 5. Construction of the multi-layered vascularized skin substitute. (A) Construction method. (B) Sequential construction of the (i) hypodermis, (ii) small vessels, and (iii) papillary and epidermal layers, resulting in a (iv) perfusable network. Scale bar: 5 mm. Abbreviations: EC, endothelial cell; F, fibroblast; GelMA, gelatin methacryloyl; KC, keratinocytes.

an epidermal structure. The incomplete epidermis group and the complete epidermis group were both fabricated on the basis of the no epidermis group. By adjusting the printing stage temperature and path spacing, we engineered a surface with either grooves or a continuous, dense, and smooth layer. The no skin sample group was used to account for interference from water vapor inside the container. Both the Incomplete epidermis and complete epidermis groups contained the "small-micro" vascular network.

We systematically evaluated the barrier function using transepidermal water loss (TEWL) measurements, a transdermal penetration assay with a fluorescent substance, and TEER testing. As shown in Figure 7A, the TEWL test based on water absorption by color-changing silica gel demonstrated that the water retention capability of the complete epidermis group was significantly superior to that of the incomplete epidermis and no epidermis groups. This demonstrates that the dense keratinocyte layer and the intercellular substances it secretes effectively block passive water evaporation, a crucial process for maintaining the internal water balance. The impaired function of the incomplete epidermis group directly correlates with its engineered micro-grooves, which provide pathways for TEWL and molecular permeation.

The transdermal penetration assay further corroborated this observation (Figure 7B). When Dextran-FITC was used as a model molecule, its penetration rate

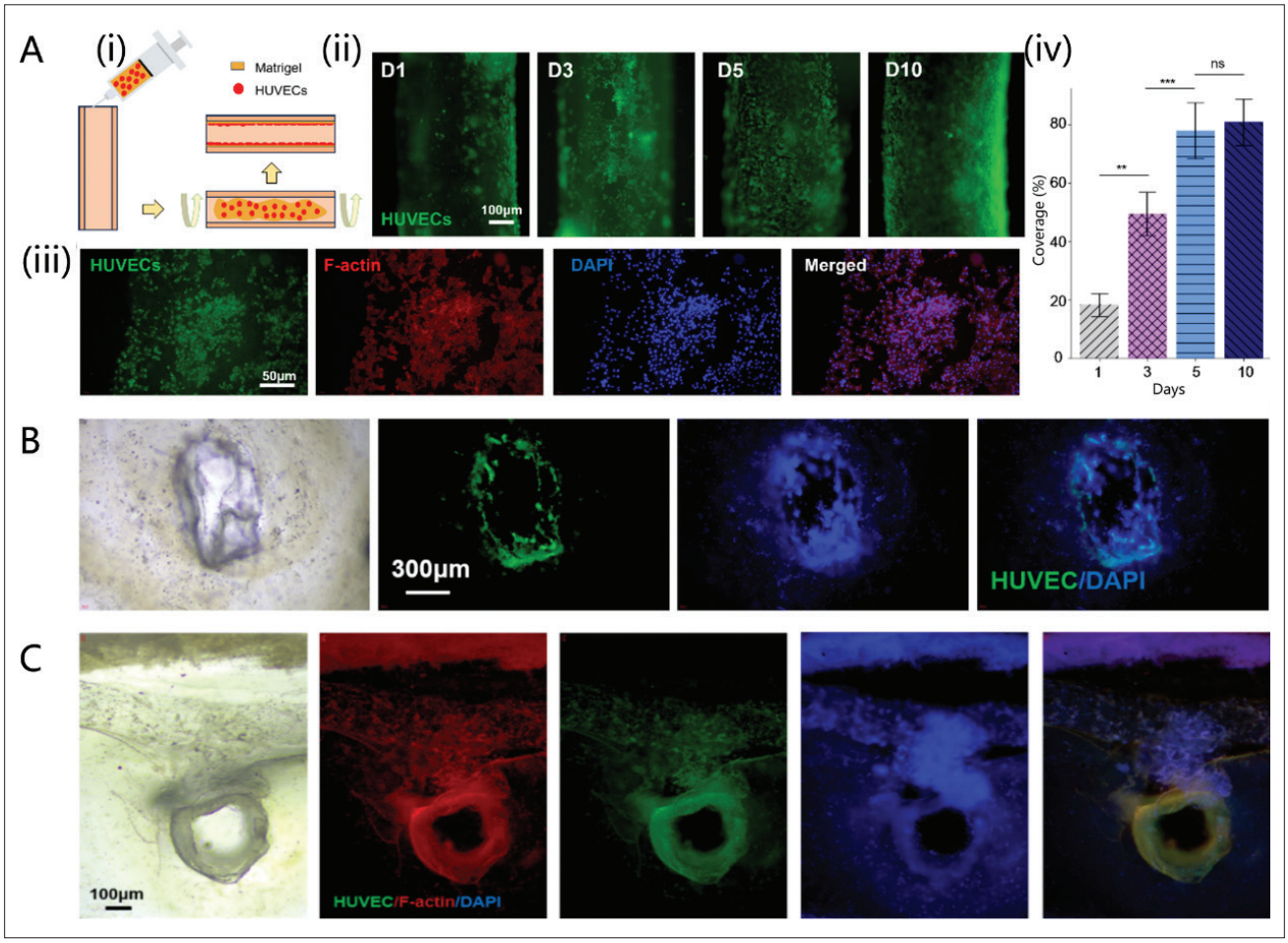

Figure 6. Characterization results of the multi-layered vascularized skin substitute. (A) Luminal adhesion of HUVECs: (i) schematic of the adhesion procedure, (ii) temporal changes in HUVEC adhesion, (iii) fluorescence staining of HUVECs, (iv) quantitative analysis of HUVEC coverage rate over time. Scale bars: 50, 100 μm; magnifications: 100×. (B) Characterization of HUVEC adhesion within the coaxial-printed small vessels. Scale bar: 300 μm; magnification: 50×. (C) Structure of the vascularized skin. Scale bar: 100 μm; magnification: 100×. Data were analyzed using one-way analysis of variance and are presented as mean ± standard deviation ($n = 3$). Statistical significance determined at $^{*}p < 0.05$, $^{**}p < 0.01$, and $^{***}p < 0.001$, while ns indicates not significant. Abbreviation: HUVEC, human umbilical vein endothelial cell.

through the complete epidermis group was the slowest, with the fluorescence intensity in the solution remaining consistently low. In contrast, the fluorescent molecules rapidly penetrated the no epidermis group, while the incomplete epidermis group showed an intermediate level, indicating that structural defects in the epidermis significantly impair its barrier efficacy. TEER testing provided electrophysiological evidence for this observation (Figure 7C). The TEER value of the complete epidermis group (3170 ± 162.35 Ω) was substantially higher than that of the incomplete epidermis group (1316 ± 182.06 Ω) and the blank control group (no skin sample) (199 ± 59.50 Ω). This 140.82% increase relative to the incomplete-epidermis group supports the conclusion that a complete and tightly connected epidermal layer is the decisive factor in establishing a high-impedance physical barrier. The results from these three experiments consistently demonstrate that the structural integrity of the epidermal layer is necessary for the engineered skin to exert an effective barrier function.

Beyond serving as a physical barrier, a functional skin substitute requires its subcutaneous vascular network to possess the capability for substance exchange. Therefore, we simulated the process of drug diffusion from blood vessels by injecting a Dextran-FITC solution into the coaxially printed small vessel within the construct and observing its extravasation behavior in real-time (Figure 7D). Time-lapse images clearly showed that the fluorescent molecules were initially confined to the vascular lumen and then gradually diffused into the surrounding extracellular matrix over time. Quantitative analysis of the

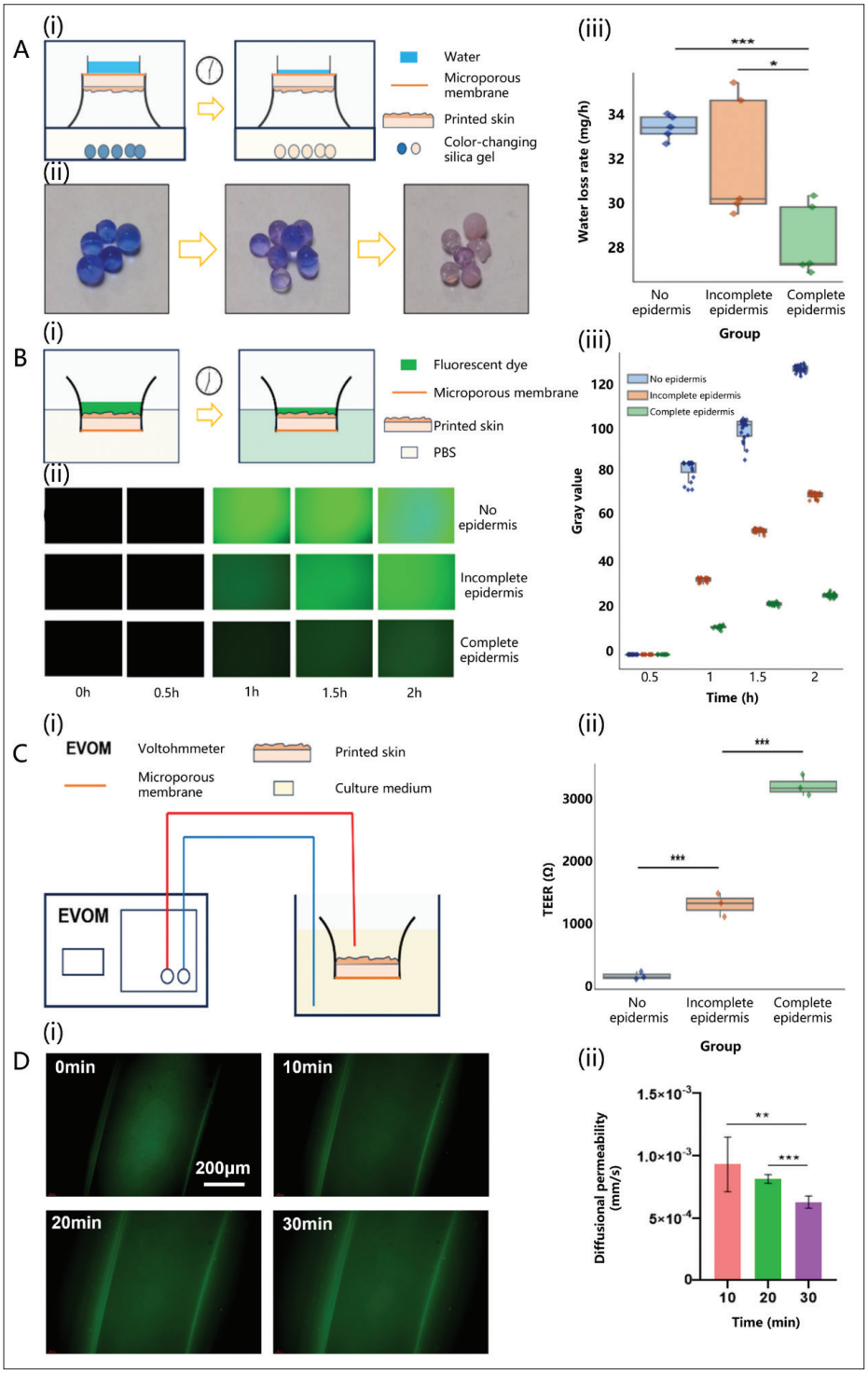

Figure 7. *In vitro* validation of the skin substitute. (A) TEWL measurement: (i) schematic of the test setup, (ii) color change of silica gel due to water absorption, (iii) water loss rate across different groups. (B) Transdermal penetration assay: (i) schematic of the test principle, (ii) fluorescence detection results, (iii) changes in fluorescence values across different groups. (C) TEER measurement: (i) schematic of the measurement principle, (ii) electrical resistance values across different groups. (D) Dextran-FITC permeability assay: (i) time-lapse images showing fluorescent molecule diffusion, (ii) quantification of diffusion rate. Scale bar: 200 μm. Data were analyzed using one-way analysis of variance and are presented as mean ± standard deviation ($n = 3$). Statistical significance determined at $^{*}p < 0.05$, $^{**}p < 0.01$, and $^{***}p < 0.001$, while ns indicates not significant. Abbreviations: Dextran-FITC, dextran–fluorescein isothiocyanate; EVO, epithelial voltohmmeter; PBS, phosphate-buffered saline; TEER, transepithelial electrical resistance; TEWL, transepidermal water loss.

diffusion rate indicated that the rate decreased over time, consistent with the classical Fick's law of diffusion,[37] where the driving force for diffusion naturally weakens as the concentration gradient across the vessel wall decreases. The hydrodynamic diameter of 40 kDa dextran is comparable to that of a key transport protein in the human body—serum albumin (approximately 66 kDa).[38] Albumin serves as the natural carrier for many hydrophobic drugs. Numerous therapeutic biomolecules, such as cytokines, enzymes, and antibody fragments, also fall within this molecular weight range. The permeation behavior of Dextran-FITC can be used to model the diffusion and clearance of these drug–protein complexes within the interstitial space and vascular system. For instance, Aflibercept (VEGF Trap),[39] a dimeric glycoprotein used to treat neovascular age-related macular degeneration, diabetic macular edema, and other angiogenic diseases, has a functional subunit size comparable to 40 kDa Dextran-FITC. Observing the diffusion of Dextran-FITC from the vascular network can directly simulate and predict the distribution kinetics and local clearance rate of drugs like Aflibercept in diseased skin tissue.

The *in vitro* functional validation demonstrates that our constructed multi-layered vascularized skin substitute not only successfully mimicked the anatomical structure of native skin but also replicated two of its core physiological functions: the excellent physical barrier function provided by the complete epidermis, and the substance transport and potential drug delivery function enabled by the multi-level hierarchical vascular network. This lays a solid foundation for its applications in wound repair, disease modeling, and *in vitro* drug screening.

3.5. Limitations and future perspectives

While the hybrid bioprinting strategy proposed in this study shows promise for constructing vascularized skin constructs, the current model still has several limitations, which also point the way for future research.

In terms of vascular function, although we achieved confluent endothelial coverage within the coaxially printed small vessels, the maturity and barrier integrity of this endothelium require further validation. For example, immunofluorescence staining for endothelial junctional proteins such as vascular endothelial cadherin and claudin-5, combined with perfusion assays using fluorescently labeled macromolecules like 70 kDa dextran, is needed to quantitatively assess vascular permeability.

Regarding tissue maturation and structural fidelity, although the current construct successfully achieved the designed spatial organization of multiple cell types, more in-depth histological analysis is still required to truly recapitulate the sophisticated layered architecture of native skin. In subsequent work, hematoxylin and eosin staining, Masson's trichrome staining, and immunohistochemical analysis should be performed to assess layer-specific markers quantitatively and evaluate tissue maturation and stratification. Relevant markers may include cytokeratin 10 for epidermal differentiation, collagen I/III in the dermal matrix, and cluster of differentiation 31 for vascular networks. Simultaneously, introducing melanocytes to model pigmentation or incorporating immune cells such as macrophages to confer immunocompetence would significantly enhance the biological relevance of this model for disease modeling and immunological studies.

For the drug delivery assessment, the diffusion kinetics of the 40 kDa Dextran-FITC model molecule provide valuable preliminary insights. However, to more accurately predict therapeutic efficacy, future studies need to directly investigate the transport and retention behaviors of clinically relevant agents. This includes small-molecule drugs, growth factors such as VEGF or basic fibroblast growth factor, as well as nanoparticle-based formulations. By analyzing the structural characteristics and permeability of the construct's vascular network and correlating them with the pharmacokinetic profiles of these agents, this model holds the potential to evolve from a structural platform into a predictive tool for preclinical drug screening.

Finally, the ultimate validation of any tissue-engineered construct lies in *in vivo* experimentation. Future work should focus on implanting these skin constructs into full-thickness skin defect models in small animals, such as mice or rats. Key evaluation metrics should include the anastomosis of the engineered vascular network with the host circulatory system, the long-term survival rate of the graft, perfusion monitoring via imaging techniques, and the wound healing efficacy compared to standard therapies. The outcomes of these experiments will lay the foundation for testing in larger, more clinically relevant animal models.

4. Conclusion

This study successfully developed a hybrid bioprinting strategy for the integrated fabrication of a multi-layered skin substitute featuring a biomimetic "small-micro" hierarchical vascular network. The 2% SA/5% GelMA composite hydrogel was optimized and validated as the coaxial printing ink. It achieved an optimal balance among rheological properties, cell adhesion, and 3D tubulogenesis capability, thus laying the material foundation for constructing functional vessels. Through systematic optimization of coaxial printing parameters combined with an ionic-photo dual-crosslinking mechanism, we achieved the automated fabrication of structurally

stable, dimensionally controllable, mechanically robust, and perfusable subcutaneous small vessels, effectively overcoming the challenges of structural contraction and instability associated with single-crosslinking methods. By integrating coaxial printing with extrusion printing technologies, we achieved, for the first time, the integrated fabrication of a full-thickness, biomimetic skin construct with designed layer compartments in a single manufacturing process. Structural characterization demonstrated that the printed construct formed a multi-level "small-micro" vascular structure and achieved the precise distribution of various cell types in their predefined locations. *In vitro* functional experiments demonstrated that the construct possessed both an effective physical barrier function and drug delivery potential enabled by the engineered vascular network, proving it to be a promising platform that integrates biomimetic architecture with initial barrier and transport functionalities.

In summary, the composite printing and dual-crosslinking strategy proposed in this study provided an effective technical solution for addressing the challenge of pre-vascularization and thick-walled tissue construction. The fabricated, multi-layered, vascularized skin substitute exhibits great potential for application in the repair of deep skin defects, disease modeling, and *in vitro* drug screening. Future work should focus on the long-term *in vivo* functional evaluation of this construct and its reparative efficacy in large animal models.

Acknowledgments

None.

Funding

This work was supported by the National Natural Science Foundation (Grant No. 82300566), the Key Science and Technology Program of Zhejiang Province (Grant No. 2023C03170 and 2023C03071), and the China Postdoctoral Science Foundation (Grant No. 2023M733095 and 2025T180562)

Conflict of interest

The authors declare no conflict of interest.

Author contributions

Conceptualization: Yichen Luo, Hao Ding, Xue Zhou
Data curation: Yichen Luo, Dan Li, Xue Zhou
Formal analysis: Yichen Luo
Funding acquisition: Bin Zhang
Investigation: Yichen Luo
Methodology: Yichen Luo, Cai Lin, Xue Zhou
Project administration: Bin Zhang
Resources: Yichen Luo
Software: Yichen Luo, Cai Lin, Xue Zhou
Supervision: Hao Ding, Xue Zhou
Validation: Yichen Luo, Dan Li, Cai Lin, Xue Zhou
Visualization: Yichen Luo, Dan Li
Writing – original draft: Yichen Luo, Dan Li
Writing – review & editing: Yichen Luo, Xue Zhou
All authors have read and agreed to the published version of the manuscript.

Ethics approval and consent to participate

Not applicable.

Consent for publication

Not applicable.

Availability of data

The data that support the findings of this study are available on request from the corresponding author.

References

1. Sen CK. Human wounds and its burden: updated 2020 compendium of estimates. *Adv Wound Care*. 2021;10(5):281-292.
doi: 10.1089/wound.2021.0026

2. Shlash SOA, Madani JOA, Deib JIE, *et al*. Demographic characteristics and outcome of burn patients requiring skin grafts: a tertiary hospital experience. *Int J Burns Trauma*. 2015;6(2):30-36.

3. Halim AS, Khoo TL, Yussof SJM. Biologic and synthetic skin substitutes: an overview. *Indian J Plast Surg*. 2010;43(Suppl):S23-S28.
doi: 10.4103/0970-0358.70712

4. Böttcher-Haberzeth S, Biedermann T, Reichmann E. Tissue engineering of skin. *Burns*. 2010;36(4):450-460.
doi: 10.1016/j.burns.2009.08.016

5. Murphy SV, Atala A. 3D bioprinting of tissues and organs. *Nat Biotechnol*. 2014;32(8):773-785.
doi: 10.1038/nbt.2958

6. Kim BS, Kwon YW, Kong JS, *et al*. 3D cell printing of invitro stabilized skin model and invivo pre-vascularized skin patch using tissue-specific extracellular matrixbioink: a step towards advanced skin tissue engineering. *Biomaterials*. 2018;168:38-53.
doi: 10.1016/j.biomaterials.2018.03.040

7. Zhang J, Yun S, Karami A, *et al*. 3D printing of a thermosensitive hydrogel for skin tissue engineering: a proof of concept study. *Bioprinting*. 2020;19:e00089.
doi: 10.1016/j.bprint.2020.e00089

8. Abaci HE, Guo Z, Coffman A, *et al*. Human skin constructs with spatially controlled vasculature using primary and iPSC-derived endothelial cells. *Adv Healthc Mater*. 2016;5(14):1800-1807.
doi: 10.1002/adhm.201500936

9. Hao L, Zhao S, Hao S, *et al*. Functionalized gelatin-alginate based bioink with enhanced manufacturability and biomimicry for accelerating wound healing. *Int J Biol Macromol*. 2023;240:124364.
doi: 10.1016/j.ijbiomac.2023.124364

10. Maggiotto F, Valle ED, Fietta A, Visentin LM, Giomo M, Cimetta E. 3D bioprinting of a perfusable skin-on-chip model suitable for drug testing and wound healing studies. *Mater Today Bio*. 2025;33:101974.
doi: 10.1016/j.mtbio.2025.101974

11. Yue K, Santiago TD, Alvarez MM, Tamayol A, Annabi N, Khademhosseini A. Synthesis, properties, and biomedical applications of gelatin methacryloyl (GelMA) hydrogels. *Biomaterials*. 2015;73:254-271.
doi: 10.1016/j.biomaterials.2015.08.045

12. Choi KY, Ajiteru O, Hong H, *et al*. A digital light processing 3D-printed artificial skin model and full-thickness wound models using silk fibroin bioink. *Acta Biomater*. 2023;164(000):16.
doi: 10.1016/j.actbio.2023.04.034

13. Daikuara L, Yue Z, Skropeta D, Wallace G. In vitro characterisation of 3D printed platelet lysate-based bioink for potential application in skin tissue engineering. *Acta Biomater*. 2021;123:286-297.
doi: 10.1016/j.actbio.2021.01.021

14. Lee KY, Mooney DJ. Alginate: properties and biomedical applications. *Prog Polym Sci*. 2012;37(1):106-126.
doi: 10.1016/j.progpolymsci.2011.06.003

15. Lee SJ, Lee JH, Park J, Kim WD, Park SA. Fabrication of 3D printing scaffold with porcine skin decellularized bio-ink for soft tissue engineering. *Materials (Basel)*. 2020;13(16):3522.
doi: 10.3390/ma13163522

16. Hakimi N, Cheng R, Leng L, *et al*. Handheld skin printer: in situ formation of planar biomaterials and tissues. *Lab Chip*. 2018;18(10):1440-1451.
doi: 10.1039/c7lc01236e

17. Gungor-Ozkerim PS, Inci I, Zhang YS, Khademhosseini A, Dokmeci MR. Bioinks for 3D bioprinting: an overview. *Biomater Sci*. 2018;6(5):915-946.
doi: 10.1039/C7BM00765E

18. Rúben P, Aureliana S, Barrias CC, Paulo B, Granja PL. A single-component hydrogel bioink for bioprinting of bioengineered 3D constructs for dermal tissue engineering. *Mater Horiz*. 2018;5(6):1100-1111.
doi: 10.1039/C8MH00525G

19. Hafa L, Breideband L, Ramirez Posada L, *et al*. Light sheet-based laser patterning bioprinting produces long-term viable full-thickness skin constructs. *Adv Mater*. 2024;36(8):e2306258.
doi: 10.1002/adma.202306258

20. Pontiggia L, Van Hengel IA, Klar A, *et al*. Bioprinting and plastic compression of large pigmented and vascularized human dermo-epidermal skin substitutes by means of a new robotic platform. *J Tissue Eng*. 2022;13:20417314221088513.
doi: 10.1177/20417314221088513

21. Kim BS, Gao G, Kim JY, Cho DW. 3D cell printing of perfusable vascularized human skin equivalent composed of epidermis, dermis, and hypodermis for better structural recapitulation of native skin. *Adv Healthc Mater*. 2019;8(7):e1801019.
doi: 10.1002/adhm.201801019

22. Huyan Y, Lian Q, Zhao T, Li D, He J. Pilot study of the biological properties and vascularization of 3D printed bilayer skin grafts. *Int J Bioprint*. 2020;6(1):246.
doi: 10.18063/ijb.v6i1.246

23. Ma J, Qin C, Wu J, *et al*. 3D Printing of strontium silicate microcylinder-containing multicellular biomaterial inks for vascularized skin regeneration. *Adv Healthc Mater*. 2021;10(16):e2100523.
doi: 10.1002/adhm.202100523

24. Nuutila K, Samandari M, Endo Y, *et al*. In vivo printing of growth factor-eluting adhesive scaffolds improves wound healing. *Bioact Mater*. 2022;8:296-308.
doi: 10.1016/j.bioactmat.2021.06.030

25. Kolesky DB, Truby RL, Gladman AS, Busbee TA, Homan KA, Lewis JA. 3D bioprinting of vascularized, heterogeneous cell-laden tissue constructs. *Adv Mater*. 2014;26(19):3124-3130.
doi: 10.1002/adma.201305506

26. Kim BS, Ahn M, Cho WW, Gao G, Jang J, Cho DW. Engineering of diseased human skin equivalent using 3D cell printing for representing pathophysiological hallmarks of type 2 diabetes in vitro. *Biomaterials*. 2021;272:120776.
doi: 10.1016/j.biomaterials.2021.120776

27. Thomas A, Orellano I, Lam T, *et al*. Vascular bioprinting with enzymatically degradable bioinks via multi-material projection-based stereolithography. *Acta Biomater*. 2020;117:121-132.
doi: 10.1016/j.actbio.2020.09.033

28. Ramasamy S, Davoodi P, Vijayavenkataraman S, *et al*. Optimized construction of a full thickness human skin equivalent using 3D bioprinting and a PCL/collagen dermal scaffold. *Bioprinting*. 2020;21:e00123.
doi: 10.1016/j.bprint.2020.e00123

29. Luo Y, Li D, Lin C, Zhou X, Ma J, Zhang B. Three-dimensional bioprinting of gelatin methacryloyl hydrogel with a tri-layered vascularized architecture for full-thickness skin regeneration. *Int J Bioprint*. 2025;11(4):328-349.
doi: 10.36922/IJB025090069

30. Zhang B, Gao L, Gu L, Yang H, Luo Y, Ma L. High-resolution 3D bioprinting system for fabricating cell-laden hydrogel scaffolds with high cellular activities. *Procedia CIRP*. 2017;65:219-224.
doi: 10.1016/j.procir.2017.04.017

31. Shao L, Gao Q, Zhao H, *et al*. Fiber-based mini tissue with morphology-controllable GelMA microfibers. *Small*. 2018;14(44):e1802187.
doi: 10.1002/smll.201802187

32. Gao Q, He Y, Fu J-z, Liu A, Ma L. Coaxial nozzle-assisted 3D bioprinting with built-in microchannels for nutrients delivery. *Biomaterials*. 2015;61:203-215.
doi: 10.1016/j.biomaterials.2015.05.031

33. Jia W, Gungor-Ozkerim PS, Zhang YS, *et al*. Direct 3D bioprinting of perfusable vascular constructs using a blend bioink. *Biomaterials*. 2016;106:58-68.
doi: 10.1016/j.biomaterials.2016.07.038

34. Riley WA, Barnes RW, Evans GW, Burke GL. Ultrasonic measurement of the elastic modulus of the common carotid artery. The Atherosclerosis Risk in Communities (ARIC) Study. *Stroke*. 1992;23(7):952-956.
doi: 10.1161/01.str.23.7.952

35. Yen RT, Fung YC, Bingham N. Elasticity of small pulmonary arteries in the cat. *J Biomech Eng*. 1980;102(2):170-177.
doi: 10.1115/1.3138218

36. Humphrey JD, Schwartz MA. Vascular mechanobiology: homeostasis, adaptation, and disease. *Annu Rev Biomed Eng*. 2021;23:1-27.
doi: 10.1146/annurev-bioeng-092419-060810

37. Fick A. On liquid diffusion. *J Membr Sci*. 1995;100(1):33-38.
doi: 10.1016/0376-7388(94)00230-V

38. Merlot AM, Kalinowski DS, Richardson DR. Unraveling the mysteries of serum albumin-more than just a serum protein. *Front Physiol*. 2014;5:299.
doi: 10.3389/fphys.2014.00299

39. Stewart MW. Aflibercept (VEGF Trap-eye): the newest anti-VEGF drug. *Br J Ophthalmol*. 2012;96(9):1157-1158.
doi: 10.1136/bjophthalmol-2011-300654